Charge carrier extraction and recombination effects in GaInAs/GaAsP multi-quantum well solar cells

View Online Export Citation CrossMark

Hasan Ahmed,[1,2] (iD) Sethulakshmi J. Sudhakaran,[2] (iD) Amani S. Almutairi,[1] (iD) Sharmistha Khan,[1] (iD)
Vincent R. Whiteside,[2] (iD) A. Petrou,[1] (iD) Ryan M. France,[3] (iD) and Ian R. Sellers[2,a] (iD)

AFFILIATIONS

[1] Department of Physics, University at Buffalo, Amherst, New York 14260, USA
[2] Department of Electrical Engineering, University at Buffalo, Amherst, New York 14260, USA
[3] National Renewable Energy Laboratory, Golden, Colorado 80401, USA

[a] Author to whom correspondence should be addressed: isellers@buffalo.edu

ABSTRACT

The carrier extraction and transport mechanisms as well as the relative contributions of radiative and non-radiative recombination processes are investigated in high-quality strain-balanced GaInAs/GaAsP multi-quantum well solar cells recently implemented in record efficiency multijunction solar cells. A comprehensive suite of complementary characterization techniques including temperature- and suns-dependent photoluminescence and photovoltaic measurements are employed to analyze thermal escape and tunneling rates, which demonstrate the need to move beyond simple drift-diffusion models of p–n junctions. This study examines the processes that best characterize the operation of these devices across varying temperatures using a simple two-diode model, incorporating multiple transport protocols, and provides insights into the performance-limiting processes and pathways for their optimization.

I. INTRODUCTION

The efficiency of single-junction solar cells is constrained by the Shockley–Queisser limit[1] due to their band gap, which restricts the absorption of sub-band gap photons and results in thermalization losses of high-energy carriers. Advanced photovoltaic concepts, such as intermediate band solar cells for sub-band gap photon absorption[2] and hot carrier solar cells for utilizing carriers excited high in the conduction band,[3] offer potential solutions but remain largely unrealized. A simpler solution to this problem is employing multijunction solar cells (MJSCs), which have seen commercial implementation in space photovoltaics where high efficiency is valued.[4] Advances in sample growth techniques have further enhanced the efficiency of single-junction cells, enabling the integration of these high-performance materials into MJSCs to mitigate both sub-band gap and thermalization losses. Much work has gone into reducing the growth defects in implementing such systems, details of which can be found elsewhere.[5–8]

A subcell of one such triple-junction MJSC is discussed here, the schematic of which is shown in Fig. 1. The full MJSC cell structure incorporating this subcell contains lattice-matched GaInP (1.9 eV) as the top layer, GaAs (1.4 eV) as the middle junction, and lattice-mismatched GaInAs (0.9 eV) with a GaInP compositionally graded-buffer (CGB) as the bottom subcell.[4] The middle subsection of such a structure, discussed herein, has 60 repeats of strain-balanced GaInAs/GaAsP quantum wells (QWs) embedded in the i-region of a p–i–n structure. The inclusion of these QWs reduces the effective band gap of the middle layer to approximately 1.35 eV, thereby extending the photon absorption range of the cell.[9] Incorporating GaInAs QWs in GaAs can, therefore, potentially increase the short-circuit current (J_{sc}) by narrowing the band gap and increasing the absorption range.[10,11]

The samples in this study were grown using metal organic vapor phase epitaxy (MOVPE). While it may be beneficial to use GaInAs QWs instead of bulk GaInAs, this comes at the expense of introducing defects due to lattice mismatch at the interface of the

barrier and quantum well regions, which are mitigated here by strain-balancing the QWs.[10] In such a process, GaInAs with its larger lattice constant is compressively strained by the GaAs substrate but this is *balanced* using GaAsP and the tensile strain this introduces, while maintaining well widths below the Matthews–Blakeslee critical thickness.[12,13] As such, the 60 QWs, therefore, are able to prevent strain relaxation while maintaining significant absorption in the intrinsic region.[4,10,14]

II. EXPERIMENTAL PROCEDURE

The quantum well solar cell device was grown by metalorganic vapor phase epitaxy (MOVPE) in a custom-built atmospheric pressure reactor on (001) GaAs substrates, miscut 2° toward (111)B. Standard III–V MOVPE precursors were used, including trimethylindium, triethylgallium, trimethylgallium, and trimethylaluminum as the group III sources, and arsine, phosphine, and dimethylhydrazine as the group V sources. Silane, diethhtylzinc, carbon tetrachloride, and hydrogen selenide were the dopant precursors. An inverted growth sequence was utilized, beginning with a GaInP stop-etch layer, a GaInNAs/GaAs:Se front contact layer, and the remaining layers shown in Fig. 1. Growth temperatures between 620 and 700 °C and growth rates between 2 and 7 μm/h were used

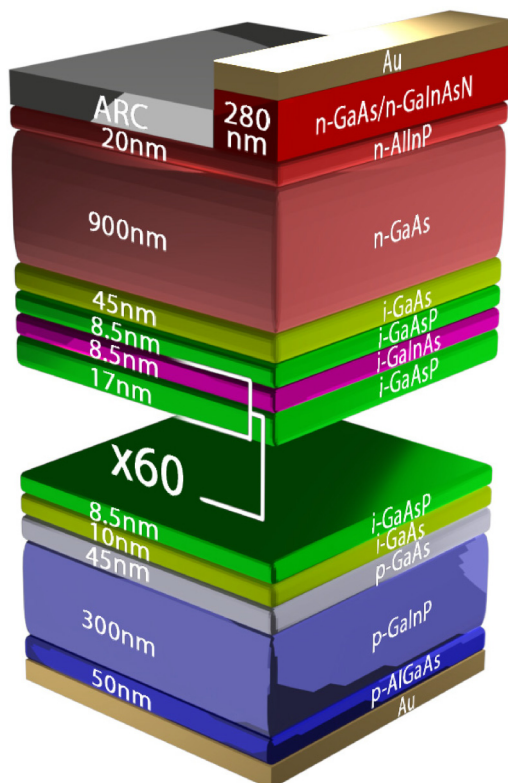for all layers, and the 8.5 nm $Ga_{0.9}In_{0.1}As$/ 17 nm $GaAs_{0.9}P_{0.1}$ layers were grown between 2.5 and 3.1 μm/h without stop-growths between layers. During growth, a k-space multi-beam optical sensor (MOS) monitored the wafer curvature of the QW layers to ensure proper stress balancing and no plastic relaxation.

The device was processed using an inverted processing sequence described previously.[15] The surface of the sample was first electroplated with planar Au, which acts both as a back contact and a reflector. The sample was then inverted and bonded onto a Si handle, and the substrate and the stop-etch layer were removed. Ni/Au front contacts were electroplated, the front contact layer was etched, the device was isolated using selective chemical etchants, and finally, a MgF_2/ZnS anti-reflection coating was deposited by thermal evaporation. The growth conditions of the sample results in "stable step bunching,"[16] details about the *in situ* curvature measurements and x-ray diffraction (XRD) can also be found here.[13]

Current density–voltage (J–V) measurements were taken using a Newport Sol3A solar simulator incorporating a 450 W Xenon lamp and an AM 1.5G filter. The sample was mounted in a LTS420E-P Linkam cryostat and LN-cooled using a Linkam LNP96 controller in steps of 10 K from 77 to 295 K. A Keithley 2400 source measurement unit (SMU) was used to sweep the voltage range both with and without illumination. Temperature-dependent external quantum efficiency measurements (EQE) were also recorded in the Linkam system in tandem with a Newport QUANTX-300 IQE/EQE instrument between 77 K and room temperature. A step size of 5 nm was used for the continuum region (400–870 nm) followed by smaller 1 nm step sizes for wavelengths >870 nm that assessed the quantum well (QW) absorption and extraction efficiency in the structure.

Sequential photoluminescence (PL) under open-circuit conditions and J–V measurements were taken between 4 K and room temperature with an unfocused 532 nm laser (the laser excitation spot size had a diameter of ~5.25 mm) at 1-sun equivalency enabled by matching the short-circuit current density (J_{sc}) under monochromatic illumination with measurements taken with the solar simulator at 295 K. The sample was placed in a Montana Instruments CryoAdvance™ 50 cryocooler and cooled in steps of 10 K from ~295 to ~4 K. The PL was recorded using a Teledyne SpectraPro HRS-300 spectrometer and a PIXIS 100 CCD camera. J–V measurements were taken after each PL scan with a Keithley 2401 SMU with and without (dark) illumination.

The QW region was simulated using $k \cdot p$ software[17] covering the 4–295 K temperature range. Parameters such as barrier height, effective mass of the confined carriers, and the barrier offset potential were extracted to calculate the thermal escape and tunneling rates of the electrons in the QWs. The electric field in the cell was estimated using a self consistent drift diffusion function to simulate the full cell structure.

III. RESULTS AND DISCUSSION

A. Photoluminescence

Temperature-dependent PL at 1-sun equivalent is shown in Fig. 2. At high temperatures ($T > 155$ K), shown in Fig. 2(a), the bulk GaAs emission dominates the PL. As expected, with increasing temperature, the PL redshifts consistent with the expected band

FIG. 1. Schematic of the strain-balanced GaInAs/GaAsP multijunction solar cell investigated in this work.

05 July 2025 07:40:02

gap variation described by Varshni[18] (Sec. 1 in the supplementary material). Notably, at lower temperatures [$T < 155$ K—Fig. 2(b)], the absence of a distinct "s-shaped" dependence in the peak position suggests minimal carrier localization states within the GaAs region of the cell, demonstrating the high quality of the samples studied here.[19] In Fig. 2(b), as the temperature is decreased, the emergence of a lower peak (∼875 nm) related to the ground-state transition in the InGaAs QW region becomes evident, eventually dominating the PL spectrum at $T < 85$ K. With further *reduction* in the temperature ($T < 85$ K), the PL is fully dominated by the QW emission with negligible emission from GaAs (these data are included in Sec. 2 in the supplementary material). The transition from the PL dominated by the QWs at low temperature to that dominated by the GaAs continuum at $T > 80$ K reflects the strong confinement and excitonic nature of the carriers at lower

temperatures and the increased influence of thermal escape of these charges as they gain increasing thermal energy at higher temperatures. Additionally, at low (85 K) to intermediate (155 K) temperatures [Fig. 2(b)], a shoulder becomes increasingly evident with increasing temperatures, energetically positioned between the bulk GaAs peak and the ground-state QW emission (∼865 nm). This feature is attributed to the emission from higher energy states in the QW that are increasingly occupied via carrier redistribution at elevated temperatures.

B. Current–voltage (J–V) measurements

Figure 3(a) shows the temperature-dependent light J–V recorded sequentially at the same conditions after each PL measurement (shown in Fig. 2), with the inset [Fig. 3(b)] showing a magnified plot of the PV regime for lower temperature data (as indicated by the dashed box in the main panel for J–V between 3.4 and 85 K). With increasing temperature, there is a significant rise in short-circuit current density (J_{sc}), increasing rapidly from 3.4 to 70 K, but more steadily thereafter. At low temperatures (inset) and high forward bias conditions (main panel), the device exhibits a current plateau in the J–V response, with the bias required to reach this current-limited state increasing with increasing temperature. This behavior suggests that a parasitic bias dependent barrier exists that inhibits carrier extraction from the QW region, which is affected by modulation of the internal electric field that affects the tunneling rates of photogenerated carriers from the QWs and/or changes in the confinement potential-inhibiting thermionic emission from the intrinsic region of the device.[20]

The inset [Fig. 3(b)] highlights the bias dependence of the monochromatic light J–V measurement at lower temperatures, which dominates carrier extraction at $T < 85$ K. Notably, as the
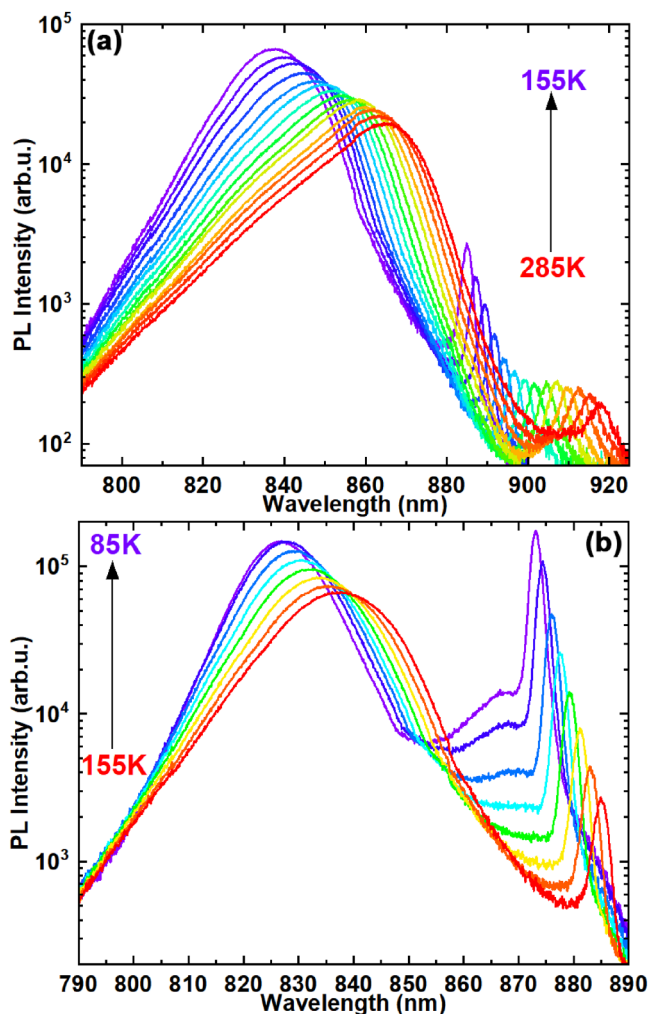

FIG. 2. Semilog plots showing (a) temperature-dependent PL from 155 to 285 K. (b) PL from intermediate temperatures (85–155 K).
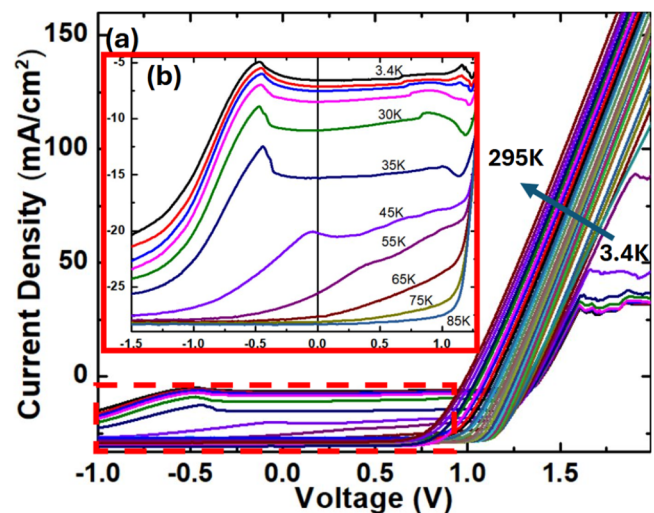

FIG. 3. (a) Temperature-dependent J–V under 1-sun equivalent monochromatic illumination at 532 nm. The inset (b) shows the PV from 3.4 to 85 K, a region highlighted by the red dashed box in the main panel.

temperature decreases, regions of negative differential resistance (NDR) emerge, particularly, in the reverse bias regime and near the forward bias diode turn-on voltage. The peak position of the NDR region in reverse bias remains relatively constant with increasing temperature up to ~35 K: however, at higher temperatures, this peak shifts toward more positive bias values. Further discussion as to the nature and temperature dynamics of this feature has been discussed with respect to transport simulations presented in Fig. 6.

C. Light J–V comparison

Figure 4 presents the temperature-dependent (TD) J_{sc} and V_{oc} extracted for the TD J–V measurements and compares those to that obtained from monochromatic excitation using a 532 nm laser at 1-sun equivalency. While the measurements taken using the solar simulator were limited to LN_2 temperatures (~77 K) by experimental constraints, the monochromatic measurements were assessed down to LHe temperatures (~4 K). The TD V_{oc} from the simulator-based J–V measurements and those from monochromatic excitation are shown as open red triangles and open green circles, respectively. Both exhibit decreasing voltage with increasing temperature, consistent with the expected behavior of the thermally mediated quasi-Fermi level separation and thermal expansion of the lattice in III–V systems. The V_{oc} data are well matched within the experimental error over the comparative range, ~80–295 K, with a room temperature V_{oc} of ~1.0 V. These data are well matched to the expected values for this system and provide added confirmation for the high material and radiative quality of this device.[4,13]

It is of note to mention the drop in J_{sc} for temperatures greater than 260 K, the cause of which has been attributed to a systematic error. Section 3 in the supplementary material shows the data from Fig. 3 with a smaller temperature range and is zoomed in to show the noise in the measurements. The measurements with

temperatures greater than 260 K show a significant increase in noise. The source of this noise may be caused by improper contacting as the temperature is raised and thermal expansion moves the contacts to a non-ideal spot on the sample.

Figure 4 also compares relative J_{sc} from the simulator derived measurements and by monochromatic excitation, along with the J_{sc} calculated from the EQE spectra convoluted with the AM 1.5G spectrum.[21] While V_{oc} provides information with respect to non-radiative losses and band gap of the absorber material, indicating high material quality for the solar cell investigated here, J_{sc} provides information related to the carrier collection efficiency and losses in device performance related to mechanisms that compete with carrier transport and extraction. As is evident in Fig. 4, the behavior of the TD J_{sc} is non-trivial and does not—over the temperature range studied—follow a typical monotonic increase related to the narrowing of the energy gap and subsequent increase absorption with increasing temperature. Rather, these data follow three clear regimes that reflect the changing and subtle nature of carrier localization, transport, and recombination driven by the carrier absorption and dynamics in the QWs. Region 1 of Fig. 4 (blue hatches) shows an order-of-magnitude increase in J_{sc}, between 4 and 85 K, which reflects the behavior presented in the inset of Fig. 3. This large change in J_{sc} indicates that carrier extraction is not driven by the conventional drift or diffusion processes but rather reflects a combination of thermally activated extraction and/or tunneling. This is supported by the J–V behavior presented in Fig. 3, which shows clear evidence of negative differential resistance (NDR) at $T < 45$ K due to the deep localization of carriers and the limited transport between the electronic levels in the QWs. This NDR is further mediated by thermal effects as the temperature increases. At low temperatures, the bulk GaAs PL quenches entirely (Fig. 2), while high radiative recombination from the e_1–h_1 ground state of the QW becomes the dominant recombination pathway. This indicates that the majority of carriers are strongly confined within the QW region at $T < 80$ K.

Region 2 (yellow hatches) and region 3 (red hatches) of Fig. 4 show comparisons of J_{sc} extracted from multiple methods including from the solar simulator (solid red triangles), via monochromatic excitation (solid green circles), in addition to convolution of the EQE and the AM1.5G spectrum (solid purple triangles).

While the thermally induced trends are qualitatively similar in all cases, and the simulator and monochromatically excited J_{sc} are well matched, those from the EQE are, in general, shifted to slightly higher values. This is attributed to systematic effects, rather than of a physical nature, that result due to the convolution of the AM1.5G standard and data in the EQE technique version vs a broad band Xe bulb excitation or monochromatic green laser illumination.

While region 1 ($T < 80$ K) shows a large change in the carrier extraction and significant quenching of the QW related PL (see Sec. 2 in the supplementary material), in region 2 (80 K < T < 150 K), J_{sc} follows a more conventional monotonic behavior that might be expected from a high-quality *bulk* solar cell that reflects the thermally induced change in the band gap and absorption edge of the device. However, when comparing the J_{sc} in region 2 with that in region 3 (150 K < T < 295 K) of Fig. 4, the behavior or dominate carrier collection process is evidently more subtle across the intermediate temperature range (80 K < T < 150 K)
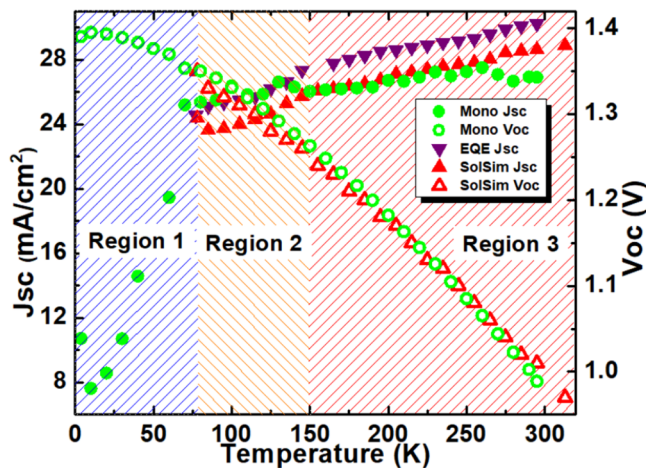

FIG. 4. Comparison of J_{sc} among 532 nm monochromatic measurements, solar simulator AM1.5G, and EQE. The V_{oc} from the former two measurements is also shown.

of region 2. To understand this behavior, the TD J–V (Fig. 3) PL and the EQE should all be considered. These *together* provide clear evidence that carrier redistribution among the QW and continuum states facilitated by increasing bias (tunneling) and temperature (thermionic emission) affect the carrier extraction, transport, and, therefore, J_{sc}. Considering this, region 2 in Fig. 4 reflects a transition regime in the devices studied, whereby the ratio of PL (carrier recombination) and J_{sc} (carrier extraction) are more balanced, and both tunneling *and* thermal excitation facilitate carrier extraction. In region 3, full escape of carriers from the QWs is achieved and the PL is dominated by the GaAs bulk within the radiative limit.

D. Quantum efficiency measurements

To further understand the nature of carrier extraction and the role of recombination in these systems, temperature-dependent external EQE was performed. The room temperature EQE is shown in Fig. 5(a) along with an inset showing the simulated energy levels of the QW structure under investigation. Several confined states are predicted, including five holes states (h_1–h_5) and an electron level (e_1), along with the less strongly confined energy levels e_2 and h_6 that energetically fall within $k_B T$ of the conduction and valence band continuums, respectively, and whose nature is, therefore, strongly modulated by the lattice temperature. *Moreover,* the EQE in Fig. 5(a) also provides evidence to suggest that there is carrier extraction from transitions related to e_2 and h_6 as shown in the dotted lines of the main panel, which indicate the positions of the various transitions predicted in the simulation. Furthermore, since strain and the strain-balanced nature of the structure are not included in the simulations, deviations from the ideal energy levels are expected. This deviation is seen most prominently in the EQE in Fig. 5(a) for the e_1–h_1 (ground-state electron to heavy hole) and

e_1–h_3 (ground-state electron to light hole) transitions, providing further evidence that strain-induced mixing of states plays a role in modifying these energy levels.

Figures 5(d) and 5(e) present different regimes of the temperature-dependent EQE; Fig. 5(d) between 245 and 295 K, and Fig. 5(e) between 195 and 235 K. The regime is presented to assess further the physical nature and origin of those data presented for regions 2 and 3 in Fig. 4. The *higher* temperature data presented in Figs. 5(d) and 5(e) enable the evolution and convolution of the two lowest energy transitions, corresponding to e_1–h_1 and the selection rule allowed e_1–h_3 transition, to be observed, and support the hypothesis that carrier redistribution among these states due to their relatively degenerate energies, particularly the heavier mass hole states, are effectively coupled as temperature increases. Here, h_1 and h_3 represent the heavy hole (HH) and light hole (LH) states, respectively, and similar HH–LH interactions to those observed in Fig. 5 have been observed in strain-balanced QW systems previously,[22] in addition to those in type-II InAs/AlAsSb systems where degenerate hole states also affect the optical absorption and recombination considerably.[23]

While tensile and compressive strain in QW systems are expected to induce HH–LH splitting, an ideal strain-balanced system should exhibit no such splitting due to strain (at the strain-balancing temperature) since this behavior is mediated by non-zero strain fields. However, in InGaAs, the LH states are known to be more susceptible to perturbations in electric fields, as such the observed deviation of the h_3 LH state in Fig. 5, which is likely a manifestation of the quantum-confined Stark effect (QCSE). At lower temperatures, the EQE in Fig. 5 suggests that the states for h_1 HH and h_3 LH convolve, indicating some evidence of temperature-induced strain—resulting from the mismatch in thermal expansion coefficients between the barrier and the well—that would partially
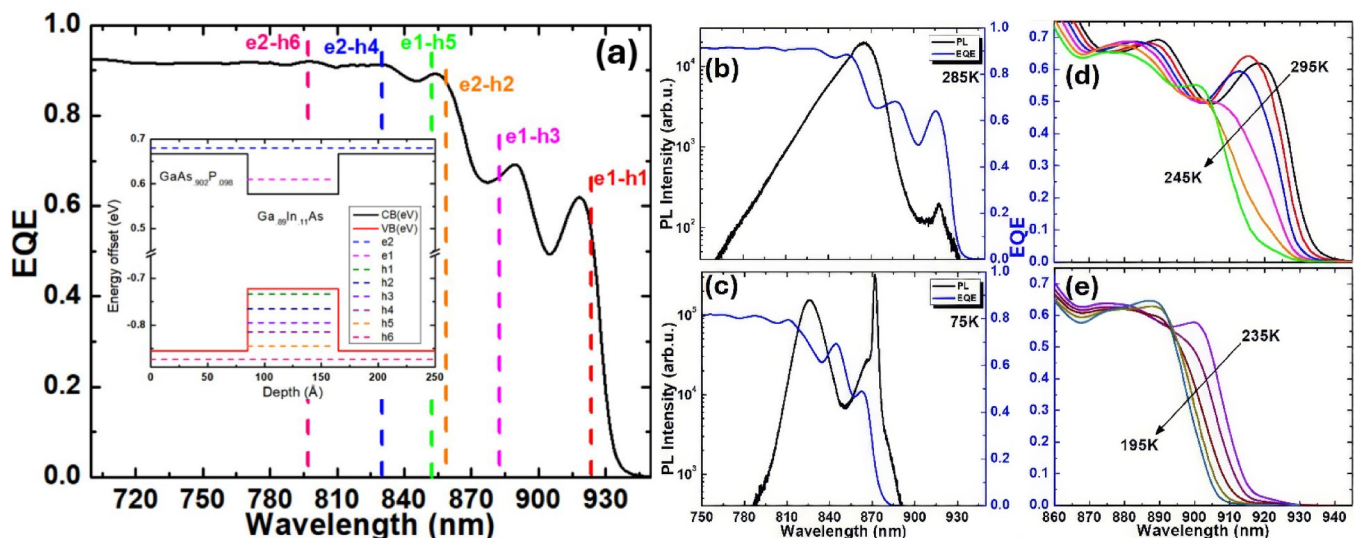

FIG. 5. (a) EQE at 295 K with energy level transitions from the simulated QW region. The inset shows the simulated QW region. (b) and (c) Shows an overlay of the semi-log plot for the PL intensity on the EQE at their corresponding temperatures. (d) and (e) EQE from 295 to 245 and 235–195 K, respectively.

counteract the perturbative effects of the electric field. It should be noted that the sample was strain-balanced at growth temperatures, and while a difference in the thermal coefficient between the barrier and the well would result in a temperature-dependent strain, this would also be true at the growth temperature. Long-range strain should be present throughout the sample due to the intrinsic material difference in the stack. This interplay highlights the delicate balance between strain, internal electric field, and thermal expansion in determining the energy states of the QW system.

It should also be noted that care must be taken to distinguish between the energy levels of the quantum well (QW) system and optical interference related to Fabry–Perot (FP) oscillations in the EQE measurements recorded here. Given that the device has a gold back contact, the presence of FP oscillations is likely. However, here, these effects appear limited—or are not dominant—when considering the *temperature-dependent* (TD) shifts observed in the extraction of the peaks in the EQE data. This suggests that the shifts in the EQE resonances with temperature arise from band gap variations rather than optical interference. If the observed peaks were due to FP oscillations, a significant change in sample thickness would be required to account for the sharp peak shifts observed. As no such substantial change in thickness is expected, the features and their respective thermal shifts in the TD EQE are, therefore, attributed to the intrinsic band structure of the MQW system. To further support this conclusion, EQE was modeled using transfer matrix methods, with the results provided in Sec. 4 in the supplementary material. While the simulated EQE exhibits FP oscillations, these do not coincide with the EQE transitions related to the electronic states in the MQWs at all three temperatures and the FP resonances remain unchanged in position with respect to temperature. This further supports the hypothesis that the observed EQE peaks discussed in Fig. 5 originate primarily from the QWs rather than optical interference. For interested readers, a comparison of the EQE and the IQE at various temperatures is also given in Sec. 5 in the supplementary material. There does not appear to be any significant difference between the two in terms of the major features present.

Figures 5(b) and 5(c) show experimental comparisons between the EQE and the PL at 75 and 285 K, respectively. These data show the strong anti-correlation between the measurement's effects observed in other systems with strong excitonic nature.[24,25] This demonstrates that when confined, such as at 75 K (region 2 in Fig. 4), recombination of the photogenerated carriers in the MQWs is predominately radiative and competes with carrier extraction or useful current that would be supplied to the external load. At higher temperatures (region 3 in Fig. 4), carrier extraction from the QWs is very efficient and the PL from this region (∼920 nm) is quenched at the expense of a higher collection probability and EQE, which is now limited by the effective absorption length of the MQW system [Fig. 5(b)]. At ambient, the PL spectrum is dominated by emission from the GaAs continuum, again indicating a high material quality within the radiative limit for these devices, which is supported by the high-performance MJSC produced when implementing this MQW p–i–n diode.[1] At very low temperatures (*T* < 80 K—region 1), the PL from the MQWs dominates and the EQE from the active region of the device is negligible. This

supports the low J_{sc} evident at low temperatures and the rapid increase in carrier extraction as the thermal energy is increased in Fig. 4. The low temperature PL data are provided in Sec. 2 in the supplementary material.

E. Carrier extraction mechanisms

To further elucidate the nature of carrier transport and extraction in the systems, the barrier to extraction for electrons in the ground-state energy level was calculated along with the corresponding thermal and tunneling escape rates. The thermal escape rate can be calculated as follows:[26–28]

$$\frac{1}{\tau_{th}} = \left(\frac{1}{L_W}\right)\sqrt{\frac{kT}{2\pi\, m_W}}\exp\left(-\frac{E_b}{kT}\right), \qquad (1)$$

where τ_{th} is the thermal escape time, L_w is the QW width, m_w is the effective electron mass in the QW, and E_b is the energy barrier height for the energy electron in the ground-state quantum energy level.

A simplified version of the tunneling escape rate equation is given as follows:[27–30]

$$\frac{1}{\tau_{\mathrm{tun}}} = \left(\frac{1}{L_W^2}\right)\left(\frac{n\pi\hbar}{2m_W}\right)$$
$$\times \exp\left(-\frac{2}{\hbar}\int_0^b \sqrt{2m_b(qV(z) - E_n - qFz)}\,dz\right), \qquad (2)$$

where τ_{tun} is the tunneling escape time, n is the quantized energy index number, b is the barrier thickness, m_b is the effective electron mass in the barrier material, $V(z)$ is an arbitrary function defining the profile of the heterointerface between the quantum well and the barrier, E_n is the energy of the electron in the nth energy level, and F is the electric field in the quantum well region. For the purposes of this investigation, m_b was assumed to be the mass of the electron in a bulk system and the barrier profile $V(z)$ was simplified to a step function. The simplified outcome is, therefore,

$$\frac{1}{\tau_{\mathrm{tun}}} = \left(\frac{1}{L_W^2}\right)\left(\frac{n\pi\hbar}{2m_W}\right)\exp\left(-\frac{2\sqrt{2m_b}}{3qF\hbar}\left(E_b^{\frac{3}{2}} - (E_b - qFb)^{\frac{3}{2}}\right)\right). \quad (3)$$

Figure 6 shows the calculated thermal (solid red squares) and tunneling (solid green circles) escape rates of electrons in the QW region with respect to temperature. The simulations are once again—consistent with the TD J–V show in Fig. 4—divided into three regimes that reflect the dominate transport process. The tunneling escape rate has been shown both with (dark green circles) and without (light green circles) the assistance of the internal electric field as a result of doping in the adjacent layers. As a result of this electric field, the tunneling rate is enhanced by several orders of magnitude, coinciding with the thermal escape rate at a higher temperature of 170 K. This is, however, the ideal case: a background impurity concentration within the intrinsic QW region would reduce the electric field-aided transport. The mean electric field in the devices was estimated to be ∼7 × 10^5 V/m (details of which can be found in Sec. 6 in the supplementary material), although
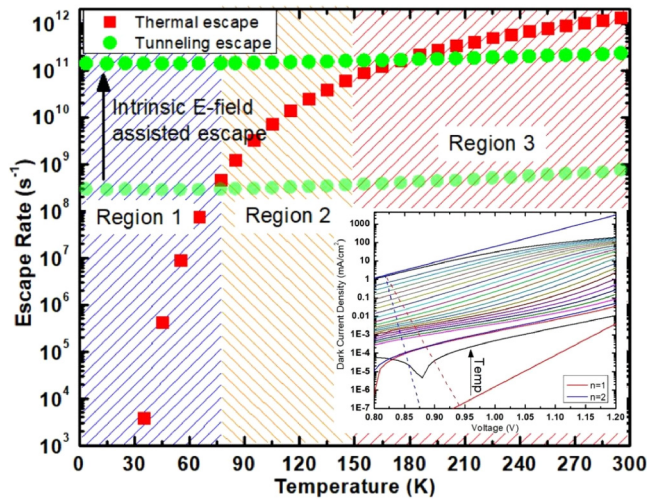
FIG. 6. Simulated calculations for thermal and tunneling escape rates for electrons in the QW region with respect to temperature subdivided into three temperature regimes. The green data points represent the tunneling escape rate of the electrons with an arrow accounting for the shift in this rate if field-aided escape is included. The inset shows a semi-log plot of the temperature-dependent experimental dark J–V alongside the theoretical model for dark J–V according to the diode equation with ideality factors, $n = 1$ (diffuse) and 2 (generation-recombination). The ideal $n = 1$ and $n = 2$ responses are shown in solid red and blue, respectively, for comparison. Also shown in the inset are dashed lines that are normal to the ideal $n = 1$ (dashed red) and $n = 2$ (dashed blue) to facilitate the ease in observation of deviations from these ideals in the experimental data.

variations in field magnitude across the device can alter or affect the effective barrier lowering near "flatband" conditions, where resonant tunneling is likely. More specifically, differences in the electric field strength across the QW region would result in a difference as to the extent of the perturbation to the electron/hole energy states. This misalignment would create regions of strong confinement within the QW region and hinder the tunneling process, making thermal escape the dominant escape mechanism for a greater range of temperatures.

At the maximum power point, experimental considerations would dictate a tunneling rate closer to the case without an electric field, which is consistent with the "flattening" of the energy bands close to V_{oc} in the state-of-the-art devices as presented here. The TD J–Vs presented in Fig. 4 shows a sharp decline in J_{sc} below 70 K, where the simulation in Fig. 6 predicts a transition between thermally driven transport at $T > 80$ K and tunneling ($T < 80$ K). This indicates that tunneling is not sufficient to extract all the photogenerated carriers at low temperature in the devices investigated here. For completeness, these results can be obtained by using the average velocity of the carrier in the well by denoting a "tilt" in the well depth due to the electric field,[31–33] instead of accounting for the change in barrier height as presented here.

At J_{sc}, no bias is dropped across the cell and, as such, there remains an internal electric field within the intrinsic region of the device under these conditions. When further considering the J–V

behavior of the solar cells, as in Fig. 3, there are two bias regimes with NDR at –0.5 V and just before turn-on, indicative of tunneling, for most temperatures. Close to "turn on" in forward bias, the energy diagram of the cell is at an effectively "flatband" with the internal electric effectively quenched. This aligns the energy levels across the MQWs, enabling resonant tunneling and carrier extraction. For the case of tunneling at negative bias, Fig. 3 shows no change in the peak position of the NDR until 35 K, at these lower temperatures, the negative bias likely provides the electric field necessary to lower the barrier between the subsequent QWs in the intrinsic region, i.e., tilts the energy bands, thereby also increasing the tunneling probability. At temperatures higher than 35 K, the peak of the NDR shifts, suggesting that the electric field necessary for escape is lower due to the assistance of thermal excitation. Thus, it is fair to conclude that the escape mechanism is purely tunneling for $T < 45$ K, an interplay between thermal and tunneling, thereafter, until approximately 70 K, above which thermal escape is the more likely mechanism.

The inset in Fig. 6 shows a semi-log plot of the temperature-dependent experimental dark current density measurements alongside the theoretical model for dark current according to the diode equation with ideality factors, $n = 1$ and 2. The perpendicular to these modeled equations has been shown in dotted lines to emphasize the deviation of the slopes with respect to the experimental data. It can be observed that for higher temperatures, the J–V characteristics can be modeled using an ideality factor of 2 but these quickly deviate, requiring an ideality factor >2. For lower temperatures, this deviation is more prominent, perpendiculars to the ideal diode equations illustrate the magnitude of this deviation. This is to be expected since the ideal diode model considers conventional pn-junctions whose transport is dominated by drift or diffusion models, not p–i–n diodes with embedded QWs that require transport mediated by thermionic emission of quantum mechanical tunneling. A possible approach for low temperature measurements is to introduce more advanced tunneling diode models. To address these deviations at low temperatures, tunneling diode models such as the Simmons metal–insulator–metal (MIM) model[34] or the Tsu–Esaki quantum tunneling model[35,36] may provide a more accurate description of carrier dynamics.

IV. CONCLUSIONS

The investigation of carrier extraction and transport mechanisms in high-quality strain-balanced GaInAs/GaAsP MQW solar cells highlights the complex interplay between thermal activation and tunneling escape processes, particularly under varying temperature and electric field conditions. Temperature-dependent J–V, PL, and EQE measurements, supported by simulated calculations, reveal critical insights into the energy dynamics of the QW region and their potential impact on device performance. At higher temperatures, thermal escape is the dominant mechanism for carrier extraction, driven by the thermal excitation of carriers over the energy barrier. This is consistent with the lack of field dependence observed in the J–V characteristics at elevated temperatures and aligns with the theoretical predictions of the thermal escape rate equation. However, as the temperature decreases, the carrier escapes mechanism transitions to a tunneling-dominated process.

05 July 2025 07:40:02

The presence of negative differential resistance (NDR) in the J–V characteristics at low temperatures, particularly under reverse bias and near the flatband condition, elucidates the role of tunneling in enabling carrier transport.

Simulations further demonstrate the substantial influence of the internal electric field on tunneling rates, which can elevate tunneling escape by several orders of magnitude. However, the experimental results suggest that localized regions of reduced electric field, background impurities, and non-idealities in the barrier profile likely reduce the practical effectiveness of field-assisted tunneling. These deviations emphasize the need for careful consideration of device design, including precise control over doping, barrier uniformity, and intrinsic material quality.

Furthermore, this analysis also underscores the limitations of traditional diode models in describing the behavior of p–i–n structures with embedded QWs or nanostructures, in general. While qualitative ideal diode models with ideality factors $n = 1$ or $n = 2$ may suffice at higher temperatures, significant deviations occur at lower temperatures due to the unique transport mechanisms in MQW devices. Advanced tunneling models, such as the Simmons MIM or Tsu–Esaki quantum tunneling models,[34–37] offer more accurate frameworks for understanding carrier escape in these systems.

Overall, this study highlights the intricate balance between thermal and tunneling processes in MQW solar cells, demonstrating how temperature, electric fields, and material properties collectively influence carrier transport. These findings not only contribute to a deeper understanding of MQW solar cell behavior but also provide valuable guidance for optimizing future device designs, particularly for multi-junction solar cells operating under diverse environmental conditions such as space.

SUPPLEMENTARY MATERIAL

The conclusions of this paper are further supported by additional data provided in the supplementary material as discussed in the text.

ACKNOWLEDGMENTS

AUTHOR DECLARATIONS

Conflict of Interest

The authors have no conflicts to disclose.

Author Contributions

Hasan Ahmed: Data curation (equal); Formal analysis (equal); Investigation (equal); Methodology (equal); Writing – original draft (equal); Writing – review & editing (equal). **Sethulakshmi J. Sudhakaran:** Data curation (equal); Investigation (equal); Methodology (equal). **Amani S. Almutairi:** Data curation (equal); Investigation (equal). **Sharmistha Khan:** Data curation (equal). **Vincent R. Whiteside:** Conceptualization (equal); Data curation (equal); Formal analysis (equal); Investigation (equal); Methodology (equal); Validation (equal); Writing – review & editing (equal). **A. Petrou:** Data curation (equal); Formal analysis (equal); Supervision (equal); Writing – review & editing (equal). **Ryan M. France:** Data curation (equal); Methodology (equal); Validation (equal); Writing – review & editing (equal). **Ian R. Sellers:** Conceptualization (equal); Formal analysis (equal); Investigation (equal); Resources (equal); Supervision (equal); Validation (equal); Writing – original draft (equal); Writing – review & editing (equal).

DATA AVAILABILITY

The data that support the findings of this study are available from the corresponding author upon reasonable request.

REFERENCES

[1] W. Shockley and H. J. Queisser, "Detailed balance limit of efficiency of p-n junction solar cells," J. Appl. Phys. **32**, 510–519 (1961).

[2] H. Kum, Y. Dai, T. Aihara, M. A. Slocum, T. Tayagaki, A. Fedorenko, S. J. Polly, Z. Bittner, T. Sugaya, and S. M. Hubbard, "Two-step photon absorption in InP/InGaP quantum dot solar cells," Appl. Phys. Lett. **113**, 043902 (2018).

[3] D. K. Ferry, S. M. Goodnick, V. R. Whiteside, and I. R. Sellers, "Challenges, myths, and opportunities in hot carrier solar cells," J. Appl. Phys. **128**, 220903 (2020).

[4] R. M. France, J. F. Geisz, T. Song, W. Olavarria, M. Young, A. Kibbler, and M. A. Steiner, "Triple-junction solar cells with 39.5% terrestrial and 34.2% space efficiency enabled by thick quantum well superlattices," Joule **6**, 1121–1135 (2022).

[5] M. Yamaguchi and C. Amano, "Efficiency calculations of thin-film GaAs solar cells on Si substrates," J. Appl. Phys. **58**, 3601–3606 (1985).

[6] R. M. France, F. Dimroth, T. J. Grassman, and R. R. King, "Metamorphic epitaxy for multijunction solar cells," MRS Bull. **41**, 202–209 (2016).

[7] E. A. Fitzgerald, "Dislocations in strained-layer epitaxy: Theory, experiment, and applications," Mater. Sci. Rep. **7**, 87–142 (1991).

[8] B. W. Dodson and J. Y. Tsao, "Structural relaxation in metastable strained-layer semiconductors," Annu. Rev. Mater. Res. **19**, 419–437 (1989).

[9] J. Barnes, J. Nelson, K. W. J. Barnham, J. S. Roberts, M. A. Pate, R. Grey, S. S. Dosanjh, M. Mazzer, and F. Ghiraldo, "Characterization of GaAs/InGaAs quantum wells using photocurrent spectroscopy," J. Appl. Phys. **79**, 7775–7779 (1996).

[10] N. J. Ekins-Daukes, K. W. J. Barnham, J. P. Connolly, J. S. Roberts, J. C. Clark, G. Hill, and M. Mazzer, "Strain-balanced GaAsP/InGaAs quantum well solar cells," Appl. Phys. Lett. **75**, 4195–4197 (1999).

[11] K. W. J. Barnham, B. Braun, J. Nelson, M. Paxman, C. Button, J. S. Roberts, and C. T. Foxon, "Short-circuit current and energy efficiency enhancement in a low-dimensional structure photovoltaic device," Appl. Phys. Lett. **59**, 135–137 (1991).

[12]J. W. Matthews and A. E. Blakeslee, "Defects in epitaxial multilayers: I. Misfit dislocations," J. Cryst. Growth **27**, 118–125 (1974).

[13]P. R. Griffin, J. Barnes, K. W. J. Barnham, G. Haarpaintner, M. Mazzer, C. Zanotti-Fregonara, E. Grünbaum, C. Olson, C. Rohr, J. P. R. David, J. S. Roberts, R. Grey, and M. A. Pate, "Effect of strain relaxation on forward bias dark currents in GaAs/InGaAs multi quantum well p–i–n diodes," J. Appl. Phys. **80**, 5815–5820 (1996).

[14]M. A. Steiner, R. M. France, J. Buencuerpo, J. F. Geisz, M. P. Nielsen, A. Pusch, W. J. Olavarria, M. Young, and N. J. Ekins-Daukes, "High efficiency inverted GaAs and GaInP/GaAs solar cells with strain-balanced GaInAs/GaAsP quantum wells," Adv. Energy Mater. **11**, 2002874 (2021).

[15]A. Duda, S. Ward, and M. Young, "Inverted metamorphic multijunction (IMM) cell processing instructions," Technical Report, 2012.

[16]R. M. France, J. Selvidge, K. Mukherjee, and M. A. Steiner, "Optically thick GaInAs/GaAsP strain-balanced quantum-well tandem solar cells with 29.2% efficiency under the AM0 space spectrum," J. Appl. Phys. **132**(18), 184502 (2022).

[17]M. P. Lumb, I. Vurgaftman, C. A. Affouda, J. R. Meyer, E. H. Aifer, and R. J. Walters, Proc. SPIE **8471**, 84710A (2012).

[18]Y. P. Varshni, "Temperature dependence of the energy gap in semiconductors," Physica **34**, 149–154 (1967).

[19]J. Tang, V. R. Whiteside, H. Esmaielpour, S. Vijeyaragunathan, T. D. Mishima, M. B. Santos, and I. R. Sellers, "Effects of localization on hot carriers in InAs/AlAs$_x$Sb$_{1-x}$ quantum wells," Appl. Phys. Lett. **106**, 061902 (2015).

[20]Y. Cheng, A. J. Meleco, A. J. Roeth, V. R. Whiteside, M. C. Debnath, T. D. Mishima, M. B. Santos, S. Hatch, H. Liu, and I. R. Sellers, "An investigation of the role of radiative and nonradiative recombination processes in InAs/GaAs$_{1-x}$Sbx quantum dot solar cells," IEEE J. Photovoltaics **8**, 487–492 (2018).

[21]J. Nelson, *The Physics of Solar Cells* (Imperial College Press, 2007), p. 2007.

[22]W. Zhou, H. Shen, J. Pamulapati, P. Cooke, and M. Dutta, "Heavy- and light-hole band crossing in a variable-strain quantum-well heterostructure," Phys. Rev. B **51**, 5461–5464 (1995).

[23]V. R. Whiteside, B. A. Magill, M. P. Lumb, H. Esmaielpour, M. A. Meeker, R. R. H. H. Mudiyanselage, A. Messager, S. Vijeyaragunathan, T. D. Mishima, M. B. Santos, I. Vurgaftman, G. A. Khodaparast, and I. R. Sellers, Semicond. Sci. Technol. **34**, 025005 (2019).

[24]H. Afshari, B. K. Durant, A. R. Kirmani, S. A. Chacon, J. Mahoney, V. R. Whiteside, R. A. Scheidt, M. C. Beard, J. M. Luther, and I. R. Sellers, "0.05FA$_{0.79}$MA$_{0.16}$Pb(I$_{0.83}$Br$_{0.17}$)$_3$ solar cells," ACS Appl. Mater. Interfaces **14**, 44358–44366 (2022).

[25]M. Fukuda, V. R. Whiteside, J. C. Keay, A. Meleco, I. R. Sellers, K. Hossain, T. D. Golding, M. Leroux, and M. Al Khalfioui, "Improved performance in GaInNAs solar cells by hydrogen passivation," Appl. Phys. Lett. **106**, 141904 (2015).

[26]H. Schneider and K. v. Klitzing, "Thermionic emission and gaussian transport of holes in a GaAs/Al$_x$Ga$_{1-x}$As multiple-quantum-well structure," Phys. Rev. B **38**, 6160 (1988).

[27]Y. Dai, S. J. Polly, S. Hellstroem, M. A. Slocum, Z. S. Bittner, D. V. Forbes, P. J. Roland, R. J. Ellingson, and S. M. Hubbard, "Effect of electric field on carrier escape mechanisms in quantum dot intermediate band solar cells," J. Appl. Phys. **121**, 013101 (2017).

[28]Y. S. Dai, S. Polly, S. Hellstroem, D. V. Forbes, and S. M. Hubbard, "Electric field effect on carrier escape from InAs/GaAs quantum dots solar cells," in *2014 IEEE 40th Photovoltaic Specialist Conference (PVSC)* (IEEE, 2014), pp. 3492–3497.

[29]A. M. Fox, D. A. B. Miller, G. Livescu, J. E. Cunningham, and W. Y. Jan, "Quantum well carrier sweep out: Relation to electroabsorption and exciton saturation," IEEE J. Quantum Electron. **27**, 2281–2295 (1991).

[30]A. Alemu and A. Freundlich, "Resonant thermotunneling design for high-performance single-junction quantum-well solar cells," IEEE J. Photovoltaics **2**, 256–260 (2012).

[31]T. Nakamura, A. Fukuyama, M. Sugiyama, and T. Ikari, "Effect of strain relaxation layer insertion on carrier recombination and escaping processes in superlattice solar cell structures using photoluminescence spectroscopy," J. Phys. D: Appl. Phys **52**, 045104 (2019).

[32]K. Toprasertpong, T. Inoue, K. Watanabe, T. Kita, M. Sugiyama, and Y. Nakano, Proc. SPIE **9743**, 974315 (2016).

[33]K. Toprasertpong, T. Inoue, Y. Nakano, and M. Sugiyama, Sol. Energy Mater. Sol. Cells **174**, 146–156 (2018).

[34]J. G. Simmons, "Generalized formula for the electric tunnel effect between similar electrodes separated by a thin insulating film," J. Appl. Phys. **34**, 1793–1803 (1963).

[35]R. Tsu and L. Esaki, "Tunneling in a finite superlattice," Appl. Phys. Lett. **22**, 562–564 (1973).

[36]B. Méndez and F. Domínguez-Adame, "Numerical study of electron tunneling through heterostructures," Am. J. Phys. **62**, 143–147 (1994).

[37]M. Lotfi and D. Zohir, "PSpice implementation of a new Esaki tunnel diode macro-model," Int. J. Smart Home **10**, 153–166 (2016).